

DETERMINING HEATING TIME SCALES IN SOLAR ACTIVE REGION CORES FROM AIA/*SDO* FE XVIII IMAGES

IGNACIO UGARTE-URRA¹ AND HARRY P. WARREN²

¹College of Science, George Mason University, 4400 University Drive, Fairfax, VA 22030, USA. and

²Space Science Division, Code 7681, Naval Research Laboratory, Washington, DC 20375, USA.

Draft version June 21, 2021

ABSTRACT

We present a study of the frequency of transient brightenings in the core of solar active regions as observed in the Fe XVIII line component of AIA/*SDO* 94 Å filter images. The Fe XVIII emission is isolated using an empirical correction to remove the contribution of “warm” emission to this channel. Comparing with simultaneous observations from EIS/*Hinode*, we find that the variability observed in Fe XVIII is strongly correlated with the emission from lines formed at similar temperatures. We examine the evolution of loops in the cores of active regions at various stages of evolution. Using a newly developed event detection algorithm we characterize the distribution of event frequency, duration, and magnitude in these active regions. These distributions are similar for regions of similar age and show a consistent pattern as the regions age. This suggests that these characteristics are important constraints for models of solar active regions. We find that the typical frequency of the intensity fluctuations is about 1400 s for any given line-of-sight, i.e. about 2–3 events per hour. Using the EBTEL 0D hydrodynamic model, however, we show that this only sets a lower limit on the heating frequency along that line-of-sight.

1. INTRODUCTION

The rate at which energy is deposited in active region (AR) loops is an important constraint for heating models of the solar corona. The case has been made for both low and high frequency heating, where low frequency implies that the time interval between heating events is longer than the characteristic cooling time scales of the loops, and it is shorter than the cooling time scale in the case of high frequency. Low frequency heating has been the standard interpretation (e.g. Cargill 1994; Cargill & Klimchuk 2004) of the “nanoflare model” in which magnetic field braiding leads to coronal heating (Parker 1988).

Antiochos et al. (2003) argued that the absence of cooler loops under the soft X-ray emitting AR cores implies that there is a source of effectively steady heating that keeps those loops at high temperatures. The presence of loops at 1×10^6 K, evolving (cooling) from higher temperatures, has, nevertheless, been widely observed in other ARs (Winebarger & Warren 2005; Ugarte-Urra et al. 2006, 2009; Viall & Klimchuk 2011) suggesting that low frequency heating is also playing a role. These arguments were later developed in a more quantitative manner by determining the amount of emission at different temperature ranges and comparing them to model predictions. Again, we find in the literature support for both scenarios (e.g. Warren et al. 2011; Tripathi et al. 2011; Winebarger et al. 2011; Warren et al. 2012), suggesting that possibly both high and low frequency heating can be as important in AR loop formation. In fact, they could potentially dominate at different instances of an AR long term evolution (Ugarte-Urra & Warren 2012). Note that some concerns were raised about the limitations of the emission measure diagnostic (Guennou et al. 2013) and the implications of these uncertainties in the model interpretation (Bradshaw et al. 2012; Reep et al. 2013).

In this paper, we address the problem by looking directly to the time evolution of loops in ARs. We take the simple approach of looking at the intensity fluctuations at the core of active regions as a measure of the relevant time

scales for the heating. We use a newly developed algorithm to identify relevant events and extract their properties. The discretization of the lightcurves to extract statistical properties of dynamical features in the corona has been done multiple times in the past with data from various missions (*Yohkoh*, *SoHO*, *TRACE*, *Hinode*), but the focus of most of these studies has generally been in measuring the energies of the events and estimating their contributions to the overall energy budget in the corona (e.g. Shimizu 1995; Berghmans & Clette 1999; Nightingale et al. 1999; Parnell & Jupp 2000; Aschwanden & Parnell 2002; Li & Li 2010).

We take advantage of the high sensitivity and continuous high cadence observational coverage of the Extreme Ultraviolet (EUV) solar corona by the AIA instrument on board the *SDO* mission. In particular, AIA provides high cadence spectrally pure images of Fe XVIII, which has a peak formation temperature of 7×10^6 K, and a narrow temperature response, and is well suited to the characteristic temperatures of AR cores. We also apply a different strategy as we do not group pixels in space. We look at fluctuations at single pixels to get a characterization of the short-time dynamics of the overall AR.

Our study shows that the dynamics of the AR can be characterized in terms of several properties like the frequency of detected intensity enhancements (“events”), their duration and their amplitudes. We find distributions that are the same for several mature AR and note that these distributions change as the AR decays. The characteristic frequency for the events is of about 2–3 events per hour (1400 s), a time that could be interpreted as the minimum heating frequency along the line-of-sight.

2. AIA/*SDO* AND EIS/*HINODE* OBSERVATIONS

The Atmospheric Imaging Assembly (AIA) (Lemen et al. 2012) on board the *Solar Dynamics Observatory* (Pesnell et al. 2012) consists of four telescopes that take high-resolution (0.6'' per pixel) images of the full Solar disk in ten narrow-band filters at a cadence of down to 12 s. Seven

TABLE 1
AIA/*SDO* OBSERVATIONS

Target	Pass	NOAA	Start time	End time	Fied-of-view	Center [x,y]
1	1	11263	2011/08/04 20:00 UT	2011/08/05 02:00 UT	332'' × 332''	[220'', 167'']
2	1	11339	2011/11/08 14:00 UT	2011/11/08 20:00 UT	332'' × 332''	[0'', 257'']
	2	11364	2011/12/05 18:00 UT	2011/12/06 00:00 UT	332'' × 332''	[-15'', 327'']
3	1	11459	2012/04/22 00:00 UT	2012/04/22 06:00 UT	302'' × 315''	[160'', -166'']
	2	-	2012/05/18 11:00 UT	2012/05/18 17:00 UT	280'' × 256''	[64'', -225'']

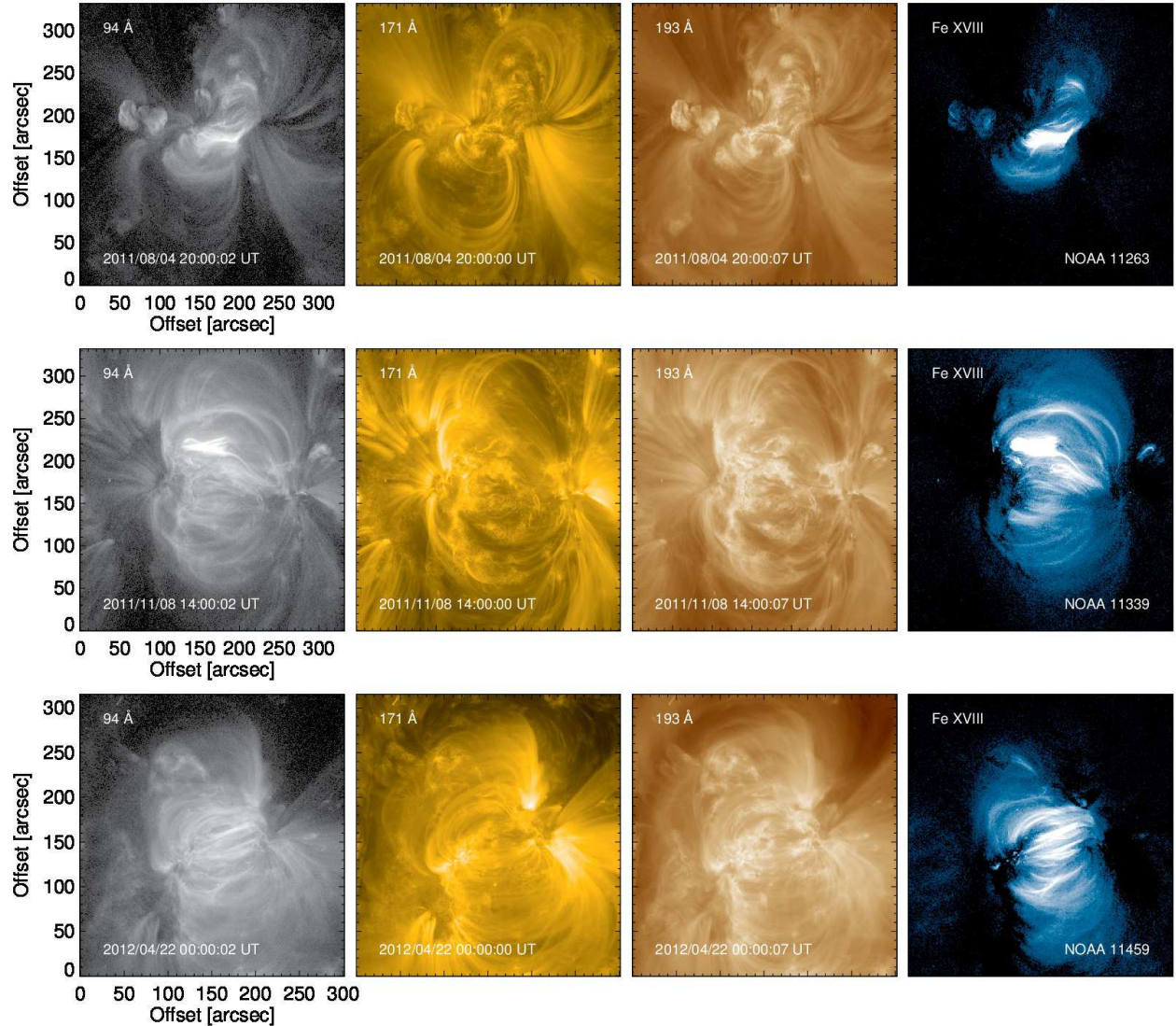


FIG. 1.— Active regions NOAA 11263, 11339 and 11459 as observed by AIA/*SDO* in their first pass on-disk. The warm contribution to the 94 Å, made out of the 193 Å and 171 Å channels, is subtracted to produce the Fe XVIII images.

of those filters image extreme-ultraviolet (EUV) bands covering a temperature range of 5×10^4 K to 2×10^7 K. The 94 Å band is centered at the spectral line Fe XVIII 93.93 Å, with a formation temperature of 7×10^6 K, that can dominate the emission in active region and flare conditions (O’Dwyer et al. 2010), as it has been shown in detailed comparisons with spectroscopic observations of active regions (Testa & Reale 2012; Teriaca et al. 2012).

Other ions like Fe X or Fe XIV (CHIANTI, Dere et al. 1997; Landi et al. 2013) are also contributors to the band, be-

coming even dominant in quiet Sun conditions, which limits the quantitative diagnostic capabilities of the channel. To circumvent this problem, Warren et al. (2012) devised an empirical method to isolate the “hot” Fe XVIII line emission from the contaminating “warm” component in the channel. The method computes the warm contribution from a weighted combination of emission from the 193 Å and the 171 Å channels, dominated by Fe XII and Fe X emission respectively. A method using only the 171 Å channel was first considered by Reale et al. (2011).

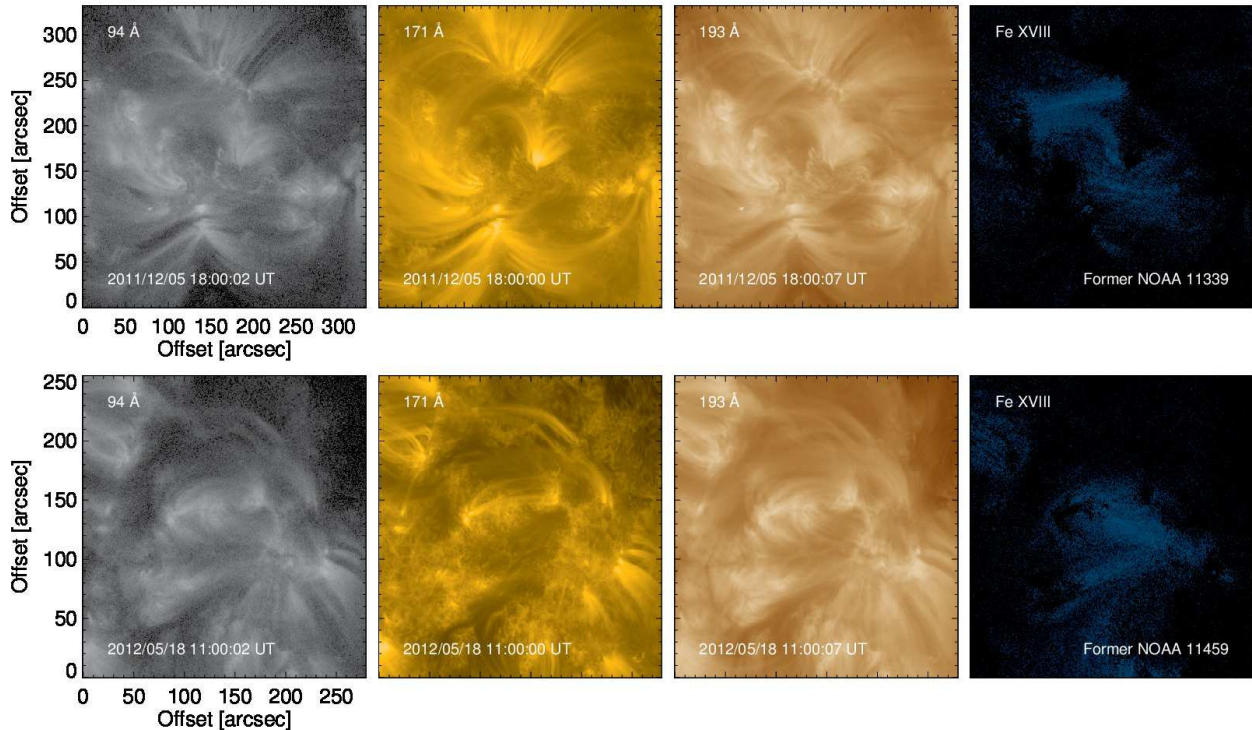


FIG. 2.— Former active regions NOAA 11339 and 11459 as observed in their second pass on-disk, one rotation later. NOAA 11459 was labeled 11364 in this pass. Same intensity scaling as in Figure 1.

While these studies demonstrated that the isolated Fe XVIII emission could be used for a quantitative analysis of active region images, to our knowledge no investigations have yet investigated the dynamics of active regions by looking into sets of consecutive images of Fe XVIII isolated emission. From now on we will refer to those images as “Fe XVIII images,” as opposed to the original “94 Å images”.

To demonstrate the applicability of the method to time dependent studies, we compared lightcurves from sequences of Fe XVIII images to simultaneous spectroscopic data from the Extreme-ultraviolet Imaging Spectrometer (EIS, Culhane et al. 2007) on board *Hinode* (Kosugi et al. 2007). The EIS is a high spatial and spectral resolution spectrograph observing in two wavelength ranges 171–212 Å and 245–291 Å. We investigated sequences of scans of a $60'' \times 368''$ area with the $2''$ slit in $4''$ steps. Each scan consists of fifteen 20 s exposures resulting in a cadence of 300 s. Data from 15 spectral windows across the two detectors were retrieved. Here we will present results from a few representative lines that cover a wide range of temperatures (1.6×10^6 K – 4.5×10^6 K): Fe XII 195.119 Å, Fe XVI 262.119 Å, Ca XIV 193.874 Å and Ca XV 200.972 Å. The data were corrected for dark current, cosmic rays, warm and hot pixels and were calibrated to absolute units using standard software. The intensities of the spectral lines were obtained from single and multiple Gaussian fits to the lines. Details about the fits and blends can be found in Ugarte-Urra & Warren (2012).

3. DATASET

We studied the dynamics of AR loops in three active regions: NOAA 11263, 11339 and 11459. The ARs were chosen from a compiled list of ARs observed by EIS using a particular observing sequence that includes a large scan with multiple spectral lines for plasma diagnostics and a sequence

of fast scans described in section 2. In a previous paper Ugarte-Urra & Warren (2012) showed that the AR core variability can change as a function of the age of the AR, with emission becoming fainter and steadier as the AR decays. Therefore, for the two ARs with a simpler long-term evolution (11339 and 11459), namely less interaction with neighboring ARs, we also looked at their dynamics one rotation later.

Each AR dataset consisted of a compilation of 6 hours worth of 94 Å, 193 Å and 171 Å level 1.0 images at a 12 s cadence and limited field-of-view. Table 1 shows the dates and times. The images were coaligned using as reference the *SDO* master pointing. To improve the signal to noise, images were then averaged to a 60 s cadence. The 193 Å and 171 Å were then used to compute and subtract the warm component contribution to the 94 Å channel (I_{94w}), resulting in a same cadence sequence of Fe XVIII images. This empirical correction is described in Warren et al. (2012) and can be summarized in these expressions

$$I_{94w} = A \sum_{i=0}^3 c_i x^i \quad (1)$$

$$x = \frac{f I_{171} + (1-f) I_{193}}{B} < I_{max} \quad (2)$$

where $A = 0.39$, $B = 116.32$, $f = 0.31$, $I_{max} = 27.5$ and $c = [-7.19 \times 10^{-2}, 9.75 \times 10^{-1}, 9.79 \times 10^{-2}, -2.81 \times 10^{-3}]$. Figure 1 shows each AR as seen in the three observed channels, plus the reconstructed Fe XVIII. Figure 2 shows NOAA 11339 and 11459 in their second pass on disk, one rotation later, with the same logarithmic intensity scaling.

4. FE XVIII TIME SERIES

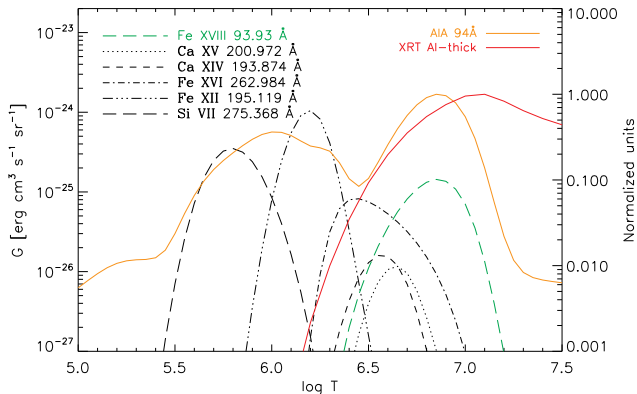


FIG. 3.— Contribution functions for Fe XVIII 93.93 Å and the spectral lines in the EIS dataset together with the normalized temperature response functions of the AIA 94 Å and the XRT Al-thick channels.

The pre-processing described above opens the door to the analysis of a unique dataset: a 60 s cadence time series of isolated Fe XVIII 93.93 Å line emission. It is unprecedented at this resolution and cadence on disk. The SUMER on board *SOHO* took spectra of Fe XIX 1118 Å at a similar cadence, but in sit-and-stare observations with a narrow slit and off-limb pointings (e.g. Tothova et al. 2011). X-ray imaging has provided imaging at a similar cadence and resolution for comparable temperatures. The relevance of isolating Fe XVIII is in its temperature resolution. Figure 3 shows the temperature response for the 94 Å channel, a typical XRT/*Hinode* filter and the contribution functions of several spectral lines including Fe XVIII.

The figure shows that the XRT filter is the most useful for the study of flare plasma at tens of million of K. For AR loops, however, the Fe XVIII line is, with the Ca lines, the best diagnostic of dynamics at the temperatures where the emission measure in AR cores peaks, 6.4–6.6 in the logarithmic scale (e.g. Warren et al. 2012). Its smaller temperature overlap with cooler lines, like Fe XII below 6.3, makes it a better discriminator of temperature changes. If we attempt, as we will in the following sections, to look into the heating time scales of loops by measuring the time scales between loop brightenings, we need to be able to resolve them in time. The width of the temperature response is a fundamental factor in the duration of the brightening. When observing cooling plasma, a broader temperature response implies a longer life for the brightening, increasing the chances of overlap with preceding and trailing events and our inability to resolve them.

Similarly, the temperature where the time scale measurements are made is crucial. If the heating in loops is impulsive, as it is often interpreted from observations (e.g. Winebarger et al. 2003), theory predicts that it will heat plasma to multi million degree temperatures in the initial stages (see reviews by Klimchuk 2006; Reale 2010). As evaporation increases the density in the corona, the plasma radiates and cools, making the loops become visible in progressively cooler channels (e.g. Winebarger & Warren 2005; Ugarte-Urra et al. 2009). If the frequency between heating events is longer than the time it takes for the loop to cool below e.g. 1×10^6 K, then the radiative signatures of every heating event are detectable in channels down to those temperatures. If, however, the frequency is shorter than the cooling time, the heating events will manifest themselves in a narrower temperature range. While hotter channels, above the

cutoff where the plasma is re-heated, will be able to detect the radiative changes, the cooler ones will remain blind to that evolution. Therefore, Fe XVIII observations are more suitable to the study of heating time scales in AR loops than other cooler lines with a similar narrow temperature response.

In Figure 4 we show sample lightcurves for the 6 hour period of NOAA 11459 in its first pass on disk and NOAA 11339 in its second. The lightcurves are an integration of a $15'' \times 15''$ area and are shown in comparison to the lightcurves obtained from the EIS sequences of the same area. The figure reveals that, similarly to single images (Teriaca et al. 2012; Warren et al. 2012), the empirical correction does a good job of isolating the hotter emission in the 94 Å channel in the time series. The evolution of Fe XVIII is very similar to that of Ca XIV–XV one and much different than what is observed in Fe XII, meaning that the warm component of the channel has been successfully removed. Figure 5 shows the correlation for all pixels in the EIS-AIA overlap field-of-view and for all times, once the AIA images have been degraded to the EIS resolution. The correlation is significantly larger when comparing Fe XVIII and Ca XV than when doing it with Fe XII. Some correlation is expected in the latter because all the lines will exhibit larger intensities at the active region than in the quiet Sun. At the $1\text{--}2 \text{ DN s}^{-1}$ level, the noise starts to dominate (see inset histogram), but the right panel of Figure 4 shows that even variations at that level can be consistent with an identification of a hot Fe XVIII component at the core of the active region.

5. EVENT DETECTION

Visual inspection of the Fe XVIII movies reveals a noticeable variability in the loop structures at the core of the active region, especially when the AR is in its earliest stages of evolution. There is considerably less variability observed during the second rotation. With the goal of identifying and characterizing quantitatively the intensity variations of the loops we devised an algorithm to detect intensity enhancements in single pixel lightcurves.

The algorithm uses threshold levels to establish whether any given set of data points in the lightcurve conform an event. An event is defined as a sustained (more than three data points) intensity enhancement over the threshold. The start, peak and end times of the events are then saved for future use.

These are the main steps in the detection:

1. The lightcurves of single pixels for the full spatial domain are smoothed in time with a user defined window width (w).
2. Each lightcurve is evaluated at every single time step. A time window (Δt) is used to determine the threshold level (I_{th1}) at every time step from preceding data points. I_{th1} is calculated from the sum of the minimum intensity value within Δt , plus the standard deviation of the intensities within a user defined spatial window around that point (Δs), at the time of the minimum. The evaluation includes determining the trend of the intensity (increasing or decreasing) with respect to the last time step.
3. An intensity below the threshold moves the evaluation one time step forward (step 2). An intensity above the threshold sets the detection flag on and marks the start

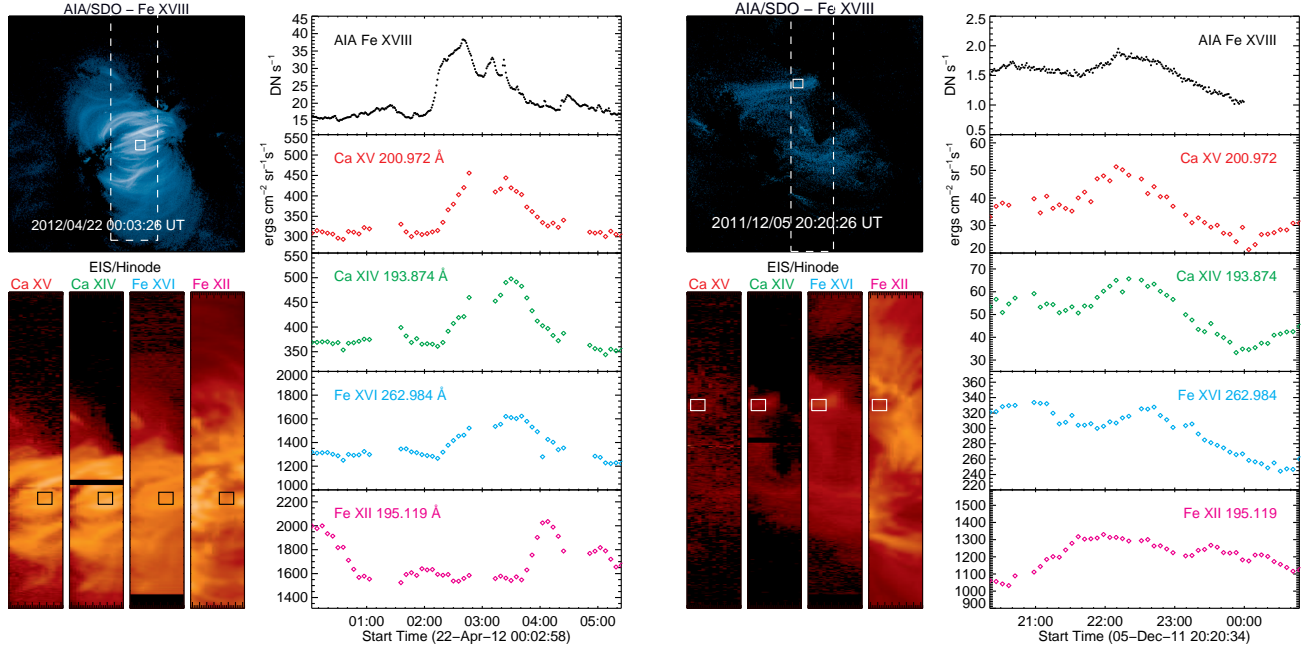


FIG. 4.— Comparison of the AIA/SDO Fe XVIII lightcurve to the Ca XV-XIV, Fe XVI-XII ones from EIS/Hinode for two active regions: NOAA11459 in its first pass on disk (left) and NOAA11339 in its second pass (right). A dashed line shows the EIS field-of-view on top of the AIA image. The solid box indicates the area of integration used for the lightcurves.

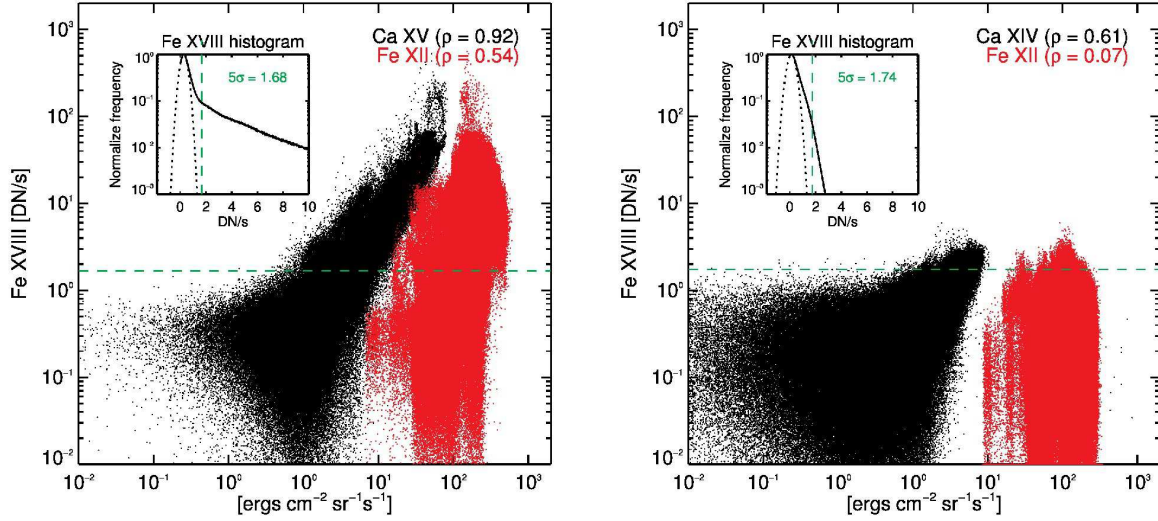


FIG. 5.— Correlation between the EIS intensities and Fe XVIII for the two datasets shown in Figure 4, i.e. all pixels in the EIS-AIA overlap field-of-view, all times. Spearman's correlation coefficient is given in brackets. Inset: histogram for the full Fe XVIII dataset with Gaussian fit (dotted line) of the lower end of the distribution. The green dashed line was used as the noise threshold level in the event detection.

- of the event and determines its peak time (maximum intensity).
- The peak time is re-evaluated at every time step when the detection flag is on and the trend is increasing.
 - In a decreasing trend, the detection flag is set off when the intensity falls below I_{th1} . Its end time is then recorded. Alternatively, a second threshold I_{th2} is defined when a decreasing intensity trend switches to an increasing one resulting in a local minimum. A new event is started if the intensity is greater than I_{th2} . New start and peak times are then defined. The detection flag

is set off when the decreasing intensity falls below I_{th2} .

In our analysis w was set to 5 data points (300 s) to avoid detections due to the one short-term variability from photon noise. As it will be shown later, this does not fully prevent the detection of noise. Δt was set to 10 data points and Δs to 1, so that the standard deviation is calculated from the eight neighboring spatial pixels. $I(t) + I_{th}$ were forced to be larger than the noise threshold for the image ($\approx 1.8 \text{ DN s}^{-1}$, see Figure 5).

Figure 6 shows representative smoothed lightcurves with detections from the algorithm for several pixels with different

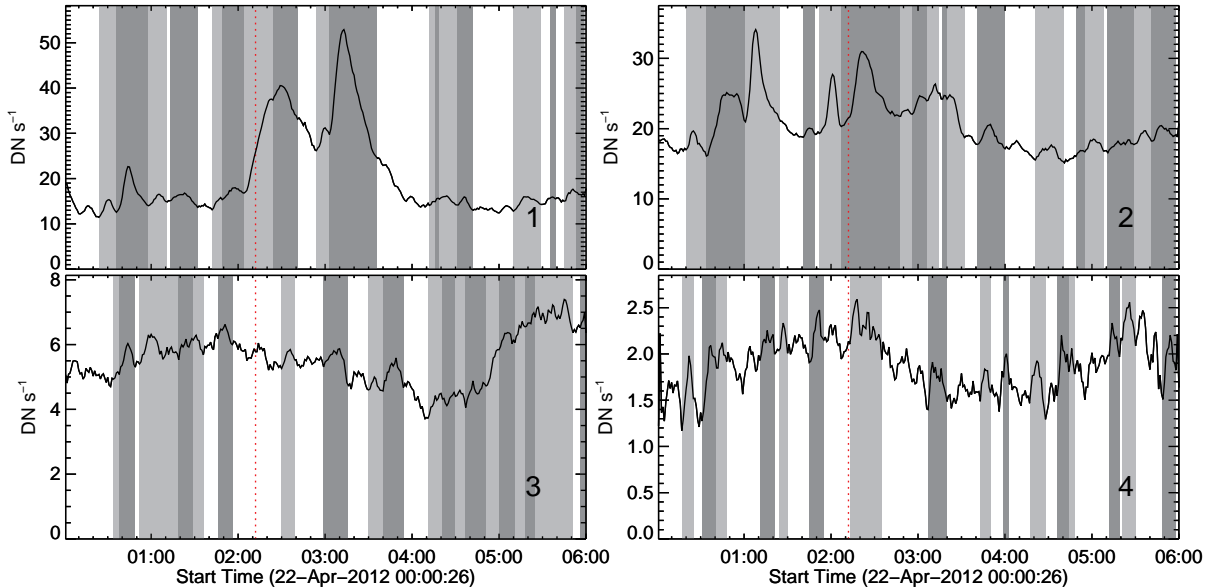


FIG. 6.— Fe XVIII smoothed lightcurves for the four marked locations in NOAA 11459 in Figure 7. Shaded in gray are the events detected by the algorithm. The red dotted line indicates the time corresponding to images shown in Figure 7.



FIG. 7.— Spatial representation of the detection algorithm outputs in the first pass of NOAA 11459. Left: input intensities; middle: map of detections at a given instant; right: map of the events' phases, where time elapsed in event is normalized by duration.

intensity levels in the NOAA 11459 dataset. In those pixels with high signal to noise (1 and 2) the algorithm does a good job of identifying events that would have been selected in a visual inspection. As the photon noise becomes more important (3 and 4), lightcurves become more jagged and the algorithm results only partially agree with a visual identification. As is discussed in more detail in the next section, some of these detected events are a result of the noise. This performance is satisfactory for our purposes, as we are particularly interested in having a characterization of the core of the AR where the Fe XVIII signal is high. Whatismore, the ultimate goal is to compare the results of this sort of analysis done both in observations and full active region simulations. In such a comparison, the key is having the same characterization of the dynamics, independently of how successful the identification of single events is.

Figure 7 shows the results of the detection for a given instant in the first pass of NOAA 11459. The right panel shows

the phase of each event color-coded. The colors are assigned based on the time elapsed since the start of the event, normalized by the duration. Elongated stretches of pixels in the same phase demonstrate that the algorithm is able to detect the evolutionary properties of loop structures from the independent study of single pixels.

6. EVENTS DYNAMICS

The start, peak and end times of every event, as well as the intensity increase from start to peak in DN s^{-1} are saved for statistical analysis. The number of events, multiple per lightcurve with several thousand lightcurves per dataset, allows us to look into the statistics of the active region dynamics as observed in the Fe XVIII line.

As we are interested in the heating frequency at any location, we first quantified the frequency of events per lightcurve, namely the number of events per hour at a single pixel location and for all pixels in an AR. Left panel in Figure 8 shows

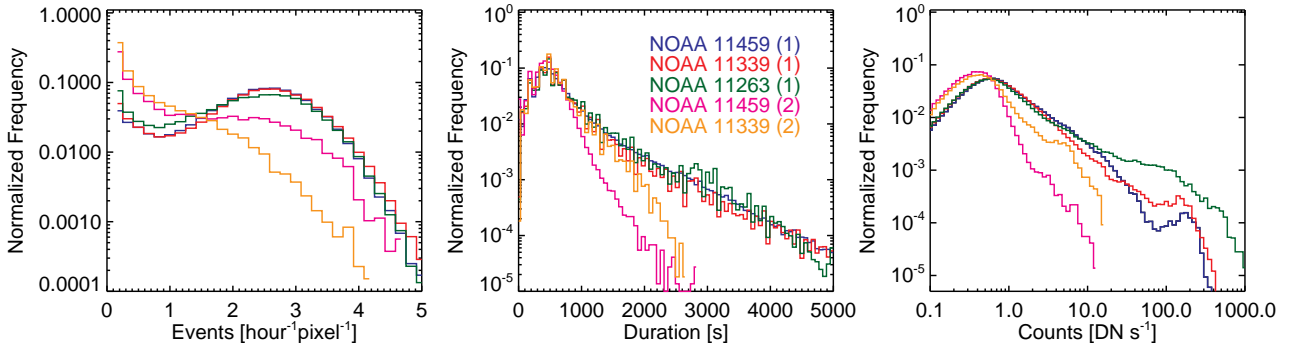


FIG. 8.— Event properties from the analysis of three AR datasets on the first pass on disk and the two on the second pass. Left panel: histogram of the number of events per lightcurve at every pixel location; middle: distribution of event durations; right: distribution of intensity enhancements. Pass number in brackets.

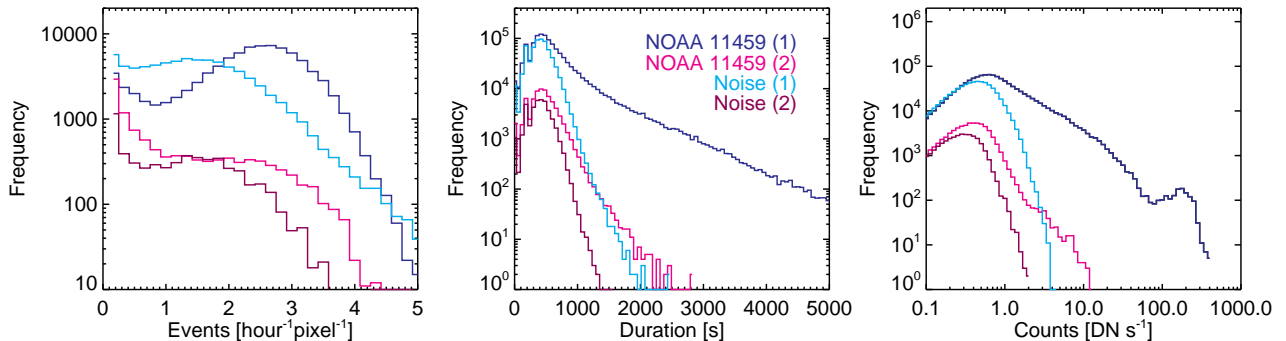


FIG. 9.— Comparison of the properties for events detected on the NOAA 11459 datasets, in two stages of evolution, to the properties of events detected from simulated sequences where fluctuations are only due to noise.

the histograms for all three AR datasets in their first pass on disk and also in the two with a second pass. We also determined the duration of all the events and the intensity increase associated to each of them. These are shown in the middle and right panels of the figure.

The first thing to notice is that all three ARs exhibit very similar properties in the early stages of evolution, with nearly identical event distributions. Those distributions change noticeably for the second pass on disk. The typical number of events in the 6 hour time span is around 15–16 events. This represents about 2.5 events per hour or an event every 1400 s. Sample lightcurves 1 and 2 in Figure 6, at the core, have 18 events each (1200 s). The distributions show that small events are the most frequent, as well as those that are short. Short and small events can be due to noise fluctuations in the lightcurves. To investigate the role that the detection of noise could play in our sample, we constructed a simulated “noise-only” dataset for each AIA observation, where the base image is the median intensity image for the time series, and the fluctuations in time are random intensity additions from a normal distribution centered at 0 and with a standard deviation equal to the characteristic uncertainty for that intensity. The relationship between different intensity levels and noise was obtained from the errors, calculated in turn from the standard deviation of the five 12 s cadence images averaged to make the 1 minute final cadence. We find that estimates of the uncertainties provided by the standard AIA processing software are conservative with respect to our own estimate.

Figure 9 shows a comparison of the results from the detection algorithm in the AIA data to the results of the simulated data, revealing that, in fact, noise fluctuations are detected by our algorithm and their characteristics are identifiable in the real data distributions. They also expose that while

noise dominates the fluctuations detected on the low signal second pass on-disk, there is a distinct variability that can be attributed to intrinsic variations in the loop structures, with noticeable differences with respect to the early stages of evolution and reproducible for different ARs. Discrepancies in the variability of ARs at the different stages of evolution had already been noted by Ugarte-Urra & Warren (2012).

We should, however, be careful with extracting too many conclusions from the duration and count distributions, because these are statistics for events on single pixel lightcurves. As loops stretch along multiple pixels, single heating events manifest themselves multiple times in the distributions given more weight to the properties of intensity enhancements in long loops. Other studies have addressed this issue by defining events not only by the evolution of the lightcurves in time, but also in space, grouping pixels with similar evolution. While we find this a valid approach, we prefer a strategy where there are no assumptions about the relationship between different volumes of emission. Instead of justifying that every detection of the code is a single heating event, which could be true in time, but not in space due to the effectiveness of thermal conduction along the loop, our strategy is to develop a code that can characterize the short-term dynamics at the core of an AR. This characterization can later be compared to a model of the atmosphere that attempts to reproduce the observations. Here we have demonstrated that this characterization can be valid for different active regions attending to the evolutionary stage.

7. DISCUSSION

Our results indicate that there are intensity enhancements at a frequency of around 2–3 events per hour along any given line-of-sight. Interpreting intensity enhancements in

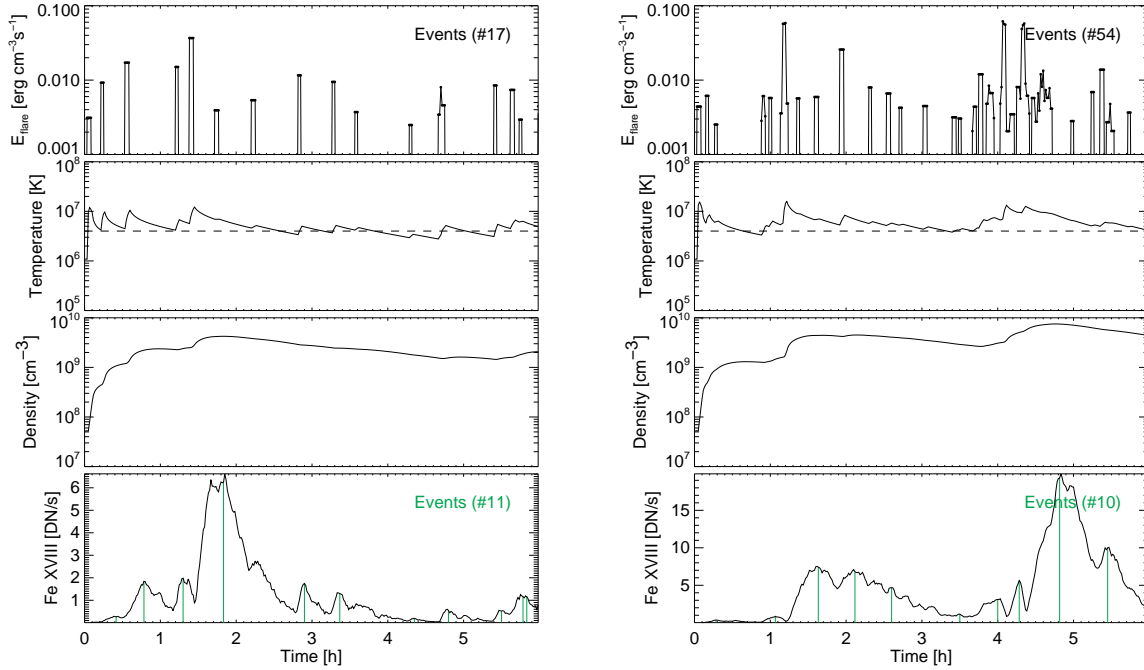


FIG. 10.— EBTEL 0D hydrodynamic simulations of a 100 Mm loop, 500 km radius. In the left panel case, the heating frequency is comparable to the frequency of events found in the AR observations. On the right panel, the frequency is three times larger. Note the resulting Fe XVIII lightcurves are comparable in terms of smoothness and number of events.

loop structures as signatures of heating events that change the plasma properties in the corona is a common and reasonable assumption. Observed intensity changes in a particular waveband can be a consequence of density or temperature variations in the plasma. Both occur in loop evolution. Loops come and go and when present their electron density is larger than the background corona as measured from spectral line ratios. Also the presence of temperature variations has been unambiguously determined from looking at their sequential evolution in different channels sensitive to different temperatures.

To investigate what can be inferred about the heating frequency from these results, we will use a zero-dimensional hydrodynamic coronal model called “Enthalpy-based Thermal Evolution of Loops” (EBTEL; Klimchuk et al. 2008; Cargill et al. 2012). The model, benchmarked with the Hydrad 1D hydrodynamic code (Bradshaw & Mason 2003), computes spatially averaged loop properties like the electron density and temperature, as a function of time, given an ad hoc heating rate function.

As a first test, we computed the temperature and density evolution of a typical loop structure that is heated repeatedly at a frequency of about 18 events per 6 hour stretch, i.e. 3 events per hour. We chose a square heating function with random amplitudes obtained from a power-law distribution $N(E)dE = E^\alpha$, $\alpha = -2$ and a 200 s event duration. The energies range was set to reach the typical 4×10^6 K temperatures found at the core of ARs. The times were randomly calculated from a normal distribution of time intervals centered at 1200 s and a width of 1000 s. The loop length was set at 100 Mm, measured from the footpoints separation of the Fe XVIII loops and assuming semicircular shape. To render the Fe XVIII intensities from the electron density and temperature, we assumed a loop radius of 500 km (Brooks et al.

2012).

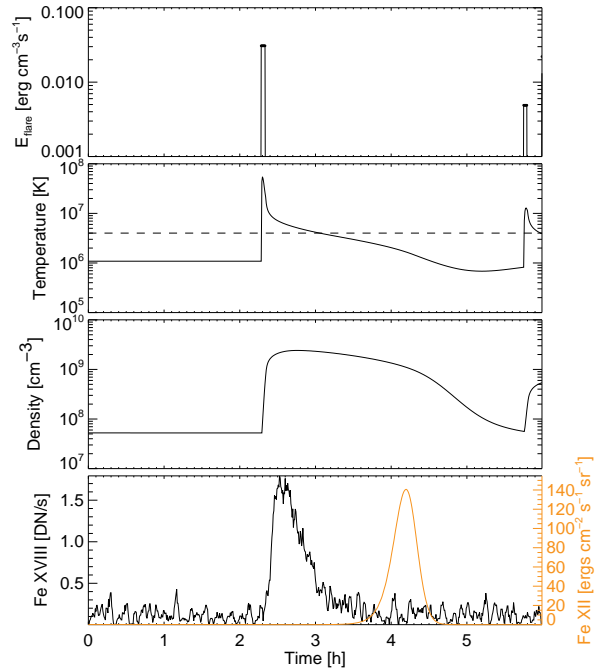


FIG. 11.— EBTEL simulation of a 100 Mm loop with low frequency heating. The bottom panel shows the Fe XVIII and Fe XII lightcurves as the loop cools.

The left panel on Figure 10 shows the time evolution of the density, temperature and predicted Fe XVIII counts for a loop heated at that frequency. That cadence of heat deposition is

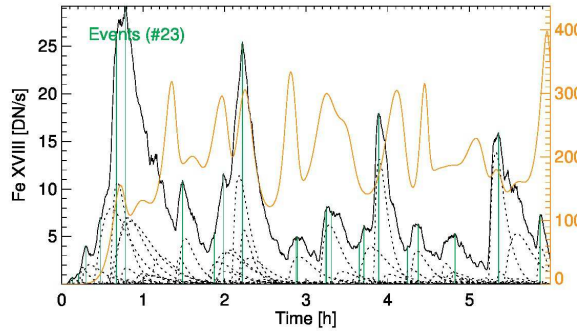


FIG. 12.— Simulated Fe XVIII and Fe XII envelope lightcurves from the integration of the emission produced by 200 low-frequency heating loops along a given line-of-sight. In green the events detected by the algorithm. The dashed lines represent the Fe XVIII lightcurves in individual loops.

sufficient to keep the loop at around 4×10^6 K not allowing it cool, making the heating effectively steady despite its impulsive nature. It is also interesting to note that the number of events retrieved by the detection algorithm from the Fe XVIII lightcurve is inferior to the actual number of heating events needed to produce it. In the simulated observations we see an envelope of the emission that hides some of the events due to the superposition of the Fe XVIII responses to the each of them, plus the smearing due to the noise and the smoothing window of the processing. This is demonstrated further when we run the same simulation with three times the number of heating events (right panel in Figure 10) and we obtain a similar number of detections. We can safely conclude then that the frequency we have measured in our AR dataset is just a lower limit of the actual heating frequency along the line-of-sight.

It is very unlikely, however, that there is only one loop emitting along a given line-of-sight. The most likely scenario is that there are multiple loops. We have simulated such a scenario considering this time loops that are heated impulsively and at a low frequency, a frequency that allows them to cool down to million degree temperatures (see Figure 11). We have considered 200 loops heated with the same heating function as before, but with a frequency of 2–3 random events per six hour stretch. Adding up the Fe XVIII emission of all those structures, we obtain an envelope lightcurve (Figure 12) that resembles the ones described in the single loop test. The number of detected events is again smaller, significantly this time, than the actual number of heating depositions along the line-of-sight.

This comparative analysis of real and simulated lightcurves reinforces the intuitive idea that counting events from integrated emission along a likely plasma filled line-of-sight, like

the core of an AR, provides only partial clues about the properties of the heating. The line-of-sight effects and their implications for coronal heating have also been discussed recently by Viall & Klimchuk (2013). Our analysis can be a complement to other diagnostics like the emission measure distribution (DEM) along the line-of-sight. The DEM has already been used as a potential discriminator for the heating frequency by establishing the different contribution levels for the emission and different temperatures very dependent on whether the plasma is heated repeatedly and not allowed to cool or more sporadically allowing for emission at all temperatures (see discussions in Warren et al. 2011; Tripathi et al. 2011; Mulu-Moore et al. 2011; Ugarte-Urra & Warren 2012; Bradshaw et al. 2012).

8. CONCLUSIONS

We present the analysis of unique spectrally pure Fe XVIII AIA/SDO high spatial resolution and high cadence observations of three ARs in different stages of evolution. The formation temperature of this line makes it an ideal candidate to study the properties of the heating time scales at the core of AR. We demonstrate our ability to isolate the line and study the intensity fluctuations in time down to very low count rates. We then construct an algorithm to quantify the observed variability by counting the number of transient brightenings (events), that could be a proxy for heating events.

We find that the ARs investigated show reproducible traits in their variability like the number of detected events during the same span of time, resulting in a characteristic frequency of about 2–3 events per hour (1400 s) for any given line-of-sight view. We show that, while this is a constrain on the maximum time between heating events, the frequency of the heating could be significantly higher, as we can only detect events from the envelope lightcurve. This envelope can be the result of the integration of many smaller events.

Furthermore, these detected events have duration and strength distributions that are very similar for different ARs, making them a potentially testable constrain for full active region time dependent models. We, therefore, suggest that a promising avenue to circumvent the inherent limitations of characterizing the time scales of the heating through line-of-sight integrated emission difficult to deconvolve, is to apply the statistical analysis techniques used on real observations to the forward modeling results of full active region heating.

The authors acknowledge funding from NASA grant NNX13AE06G through the ROSES 2012 Program NNX12ZDA001N-SHP. AIA data is courtesy of NASA/SDO and the AIA science team. Hinode is a Japanese mission developed and launched by ISAS/JAXA, with NAOJ as domestic partner and NASA and STFC (UK) as international partners. It is operated by these agencies in co-operation with ESA and NSC (Norway). CHIANTI is a collaborative project involving George Mason University, the University of Michigan (USA) and the University of Cambridge (UK).

REFERENCES

- Antiochos, S. K., Karpen, J. T., DeLuca, E. E., Golub, L., & Hamilton, P. 2003, *ApJ*, 590, 547
 Aschwanden, M. J., & Parnell, C. E. 2002, *ApJ*, 572, 1048
 Berghmans, D., & Clette, F. 1999, *Sol. Phys.*, 186, 207
 Bradshaw, S. J., Klimchuk, J. A., & Reep, J. W. 2012, *ApJ*, 758, 53
 Bradshaw, S. J., & Mason, H. E. 2003, *A&A*, 401, 699
 Brooks, D. H., Warren, H. P., & Ugarte-Urra, I. 2012, *ApJ*, 755, L33
 Cargill, P. J. 1994, *ApJ*, 422, 381
 Cargill, P. J., Bradshaw, S. J., & Klimchuk, J. A. 2012, *ApJ*, 752, 161
 Cargill, P. J., & Klimchuk, J. A. 2004, *ApJ*, 605, 911
 Culhane, J. L., et al. 2007, *Sol. Phys.*, 243, 19
 Dere, K. P., Landi, E., Mason, H. E., Monsignori Fossi, B. C., & Young, P. R. 1997, *A&AS*, 125, 149

- Guennou, C., Auchère, F., Klimchuk, J. A., Bocchialini, K., & Parenti, S. 2013, *ApJ*, 774, 31
- Klimchuk, J. A. 2006, *Sol. Phys.*, 234, 41
- Klimchuk, J. A., Patsourakos, S., & Cargill, P. J. 2008, *ApJ*, 682, 1351
- Kosugi, T., et al. 2007, *Sol. Phys.*, 243, 3
- Landi, E., Young, P. R., Dere, K. P., Del Zanna, G., & Mason, H. E. 2013, *ApJ*, 763, 86
- Lemen, J. R., et al. 2012, *Sol. Phys.*, 275, 17
- Li, J.-W., & Li, H. 2010, *Research in Astronomy and Astrophysics*, 10, 696
- Mulu-Moore, F. M., Winebarger, A. R., & Warren, H. P. 2011, *ApJ*, 742, L6
- Nightingale, R. W., Aschwanden, M. J., & Hurlburt, N. E. 1999, *Sol. Phys.*, 190, 249
- O'Dwyer, B., Del Zanna, G., Mason, H. E., Weber, M. A., & Tripathi, D. 2010, *A&A*, 521, A21
- Parker, E. N. 1988, *ApJ*, 330, 474
- Parnell, C. E., & Jupp, P. E. 2000, *ApJ*, 529, 554
- Pesnell, W. D., Thompson, B. J., & Chamberlin, P. C. 2012, *Sol. Phys.*, 275, 3
- Reale, F. 2010, *Living Reviews in Solar Physics*, 7, 5
- Reale, F., Guarrasi, M., Testa, P., DeLuca, E. E., Peres, G., & Golub, L. 2011, *ApJ*, 736, L16
- Reep, J. W., Bradshaw, S. J., & Klimchuk, J. A. 2013, *ApJ*, 764, 193
- Shimizu, T. 1995, *PASJ*, 47, 251
- Teriaca, L., Warren, H. P., & Curdt, W. 2012, *ApJ*, 754, L40
- Testa, P., & Reale, F. 2012, *ApJ*, 750, L10
- Tothova, D., Innes, D. E., & Stenborg, G. 2011, *A&A*, 528, L12
- Tripathi, D., Klimchuk, J. A., & Mason, H. E. 2011, *ApJ*, 740, 111
- Ugarte-Urra, I., & Warren, H. P. 2012, *ApJ*, 761, 21
- Ugarte-Urra, I., Warren, H. P., & Brooks, D. H. 2009, *ApJ*, 695, 642
- Ugarte-Urra, I., Winebarger, A. R., & Warren, H. P. 2006, *ApJ*, 643, 1245
- Viall, N. M., & Klimchuk, J. A. 2011, *ApJ*, 738, 24
- Viall, N. M., & Klimchuk, J. A. 2013, *ApJ*, 771, 115
- Warren, H. P., Brooks, D. H., & Winebarger, A. R. 2011, *ApJ*, 734, 90
- Warren, H. P., Winebarger, A. R., & Brooks, D. H. 2012, *ApJ*, 759, 141
- Winebarger, A. R., Schmelz, J. T., Warren, H. P., Saar, S. H., & Kashyap, V. L. 2011, *ApJ*, 740, 2
- Winebarger, A. R., & Warren, H. P. 2005, *ApJ*, 626, 543
- Winebarger, A. R., Warren, H. P., & Seaton, D. B. 2003, *ApJ*, 593, 1164